



# The role of antisite defect pairs in surface reconstruction of layered $\text{AMO}_2$ oxides: A DFT + U study

A.O. Boev<sup>a</sup>, S.S. Fedotov<sup>a</sup>, A.M. Abakumov<sup>a</sup>, K.J. Stevenson<sup>a</sup>, G. Henkelman<sup>b</sup>, D.A. Aksyonov<sup>a,\*</sup>

<sup>a</sup> Skolkovo Institute of Science and Technology, Moscow 121205, Russian Federation

<sup>b</sup> Department of Chemistry and the Oden Institute for Computational and Engineering Sciences, The University of Texas at Austin, Austin, TX 78712, United States

## ARTICLE INFO

### Keywords:

Li-ion cathode materials  
Layered oxides  
Surface  
Surface defects  
DFT modeling

## ABSTRACT

Layered transition metal oxides used as cathodes in modern metal-ion batteries are prone to surface reconstruction, which is a key reason for electrochemical performance degradation. Despite extensive research on this class of materials the mechanism of surface reconstruction is still not fully clear. In this work, we use density functional theory to study the influence of antisite defect pairs on the surface structure and energetics in pristine oxide materials:  $\text{LiNiO}_2$ ,  $\text{LiCoO}_2$ ,  $\text{NaNiO}_2$ , and  $\text{NaCoO}_2$ . Wulff constructions were built to predict thermodynamically favorable surfaces and their orientation, which are in agreement with experiments. The energetics and structure were studied and compared for surface and bulk antisite defect pairs, which can be accompanied by transition metal charge disproportionation to +2 and +4, with the latter corresponding to the formation of a small hole polaron. Individual antisite complexes at the surface are found to be additionally stabilized opposite to those in the bulk, while no excess energy is released for the complete antisite-based surface reconstruction. These results provide insights for controlling the morphology of cathode particles and shed light on surface reconstructions in layered oxides.

## 1. Introduction

Transition metal layered oxides (TMOs) are one of the most important classes of cathode materials for Li/Na-ion batteries [1,2]. Li-based TMOs deliver high specific energy, fast ionic diffusivity, and good electronic conductivity; their value is increased by a relatively easy synthesis and reasonable production costs [3,4]. Despite the great success of TMOs in commercial applications, they have several serious drawbacks, which hinder further improvement of battery specific capacity and lifetime. In particular, the crystal structure of TMOs is insufficiently stable, which results in surface reconstruction and excessive reactivity with the electrolyte in a battery cell [5–7].

The importance of the surface is emphasized by the dispersed nature of a composite cathode material [8], in which micrometer-sized particles have a significant contact area with the electrolyte, allowing fast charge transfer per unit volume and short diffusion lengths for  $\text{Li}^+/\text{Na}^+$  cations [9]. The reduction in the size of particles improves the performance of the cathode material, which is, unfortunately, accompanied by a further increase of particle reactivity towards the electrolyte [10]. Several studies show that this problem can be partially alleviated through tuning of chemical composition and corresponding control of surface reconstruction [11–14]. This process is far from being fully

understood.

According to one group of experimental studies, the reconstruction occurs only after interaction with the electrolyte. These include reconstruction to spinel after cycling in  $\text{Li}[\text{Ni}_{1/5}\text{Li}_{1/5}\text{Mn}_{3/5}]\text{O}_2$  [11], to rocksalt after immersion into electrolyte of  $\text{LiNi}_x\text{Mn}_x\text{Co}_{1-2x}\text{O}_2$  [15], and to rocksalt after cycling in  $\text{Li}[\text{Ni}_x\text{Co}_y\text{Mn}_{1-x-y}]\text{O}_2$  ( $x > 0.8$ ) [12]. In the other group of experimental studies the reconstruction is observed in pristine particles after synthesis: in Li-Mn-rich oxides [16] both to rocksalt and spinel, in  $\text{LiNi}_{0.80}\text{Co}_{0.15}\text{Al}_{0.05}\text{O}_2$  to rocksalt [17], and in  $\text{NaMnTi}_{0.1}\text{Ni}_{0.1}\text{O}_2$  to spinel [13]. The reconstruction is accompanied/promoted by surface segregation of elements [18], which can have either a positive influence, such as W [12] and Ti [13], or a negative influence, such as Ni/Co [16].

To rationalize this behavior in Li and Na-based oxides, a better fundamental understanding of the structural transformations at the surface is required. However, it is complicated by a sophisticated chemical composition and experimental difficulties to study surface changes on the atomic scale. These issues can be resolved by computer modeling of simple surface transformations in pure model systems, such as  $\text{LiNiO}_2$ ,  $\text{LiCoO}_2$ ,  $\text{NaNiO}_2$ , and  $\text{NaCoO}_2$ , which are still of significant practical importance.

Both experimental and density functional theory (DFT) studies

\* Corresponding author.

E-mail address: [d.aksenov@skoltech.ru](mailto:d.aksenov@skoltech.ru) (D.A. Aksyonov).

reveal that in LiNiO<sub>2</sub> and LiCoO<sub>2</sub> the two primary surfaces are (104) and (003) [17,19,20], whereas (104) is electrochemically active due to the exposure of Li channels. Furthermore, one of the most important mechanisms of surface reconstruction is related to Li and Ni/Co exchange, known as an antisite defect [21,17], which has been addressed in recent computational studies [22–27].

In agreement with experimental data, DFT shows that the formation of  $A_M$  ( $A = \text{Li, Na, } M = \text{Ni, Co}$ ) antisite defect is easier in LiNiO<sub>2</sub> than in LiCoO<sub>2</sub> [22,23], though the possible  $A_M - M_A$  configurations and the origin of the difference between Ni and Co-based oxides are not fully clear. A few investigations consider the effect of complex compositions on AS formation in LiNi<sub>1/3</sub>Co<sub>1/3</sub>Mn<sub>1/3</sub>O<sub>2</sub> [24,28], LiNi<sub>5/6</sub>Co<sub>1/12</sub>Mn<sub>1/12</sub>O<sub>2</sub> [25], LiNi<sub>4/5</sub>Co<sub>1/10</sub>Mn<sub>1/10</sub>O<sub>2</sub> [26], LiNi<sub>1/3</sub>Co<sub>1/3</sub>Al<sub>1/3</sub>O<sub>2</sub> [28], LiNi<sub>x</sub>Mn<sub>y</sub>(Co)<sub>z</sub>O<sub>2</sub> [29], however, a systematic study of the AS interaction with surfaces for fundamental oxide systems is still missing [30].

The Na-based oxides are particularly understudied, where the relevant free surfaces are still unknown, while AS defects were considered only for NaNiO<sub>2</sub> [23,31]. The importance of such studies is justified by the recent experimental work for NaMnTi<sub>0.1</sub>Ni<sub>0.1</sub>O<sub>2</sub>, confirming that a surface reconstruction to spinel can prevent water uptake when exposed to moisture, thus improving electrochemical stability and cyclability [13].

In this paper, we attempt to fill the described gap with a systematic DFT investigation of surface energies, crystal Wulff shapes and  $A_M - M_A$  antisite defect pairs in the bulk and at the surface for LiNiO<sub>2</sub>, LiCoO<sub>2</sub>, NaNiO<sub>2</sub>, and NaCoO<sub>2</sub>. To approach surface reconstruction effects we employ a combined Monte-Carlo and atomic optimization search of the optimal surface structure considering the evolution of antisite defect pairs. The overall task is significantly complicated by the strongly-correlated nature of transition metal oxides, for which we carefully studied the effect of a small polaron localization using the DFT+U method. As a result, the total number of supercell calculations has reached one thousand and was accomplished with the help of the python-based package SIMAN for high-throughput DFT calculations [32].

In Section 2 we describe details of our calculations; in Section 3 we report on crystal and electronic structures of the considered layered oxides; and in Section 4 – energies of ideal surfaces and crystal Wulff shapes. In Section 5 we provide bulk and surface antisite defects and then end with a discussion and conclusions in Sections 6 and 7, respectively.

## 2. Computational details

The DFT calculations were performed using the projected augmented plane wave method, with the Vienna ab initio simulation package [33] and the high-throughput python-based package SIMAN [34]. We adopted the spin-polarized generalized gradient approximation (GGA) exchange–correlation functional of the Perdew, Burke, and Ernzerhof form [35]. Only ferromagnetic configurations were considered. To account for the localized nature of Ni and Co 3d electrons, the DFT+U method with a rotationally invariant approximation was used [36]. The U values were taken as 6.2 and 3.4 eV for Ni and Co, respectively [37].

The energy cutoff was 400 eV, the k-point spacing was less than 0.3 Å<sup>-1</sup>, and the maximum force acting on each atom after relaxation was less than 0.05 V/Å. For the density of states (DOS) calculation, the spacing of k-points was 0.15 Å<sup>-1</sup>. For slab calculations, only one k-point normal to the surface was used. The Gaussian smearing for Brillouin-zone integration with a smearing width of 0.05 eV was used.

To minimize artificial interactions between periodic images of defects the supercell approach with a 15 Å vacuum region was used. Convergence of surface energy is achieved as a function of the number of slab layers. The typical size of a supercell in this study is about 10 Å, corresponding to one hundred atoms on average. To guarantee accurate alignment of the Fermi energy, a dipole correction is applied normal to

the surface [38]. All slabs were constructed using the Pymatgen library appended in the SIMAN package [34]. The Wulff crystal shapes [39] were constructed using Wulffmaker software [40].

Surface energies were determined using chemical potentials obtained from phase diagrams according to

$$\gamma = \frac{E_{tot} - \sum_i n(i)\mu(i)}{2S} \quad (1)$$

where  $E_{tot}$  is the total energy of the symmetric slab with two surfaces,  $n$  and  $\mu(i)$  are the number of atoms and the chemical potential of species  $i$ , respectively, and  $S$  is the surface area. The chemical potential of the d-metals were obtained from the condition of thermodynamic equilibrium:  $\mu(A) + \mu(M) + 2\mu(O) = E(AM_2O_4)$ . Two independent chemical potentials,  $\mu(A)$  and  $\mu(O)$  allow describing the energetics of polar non-stoichiometric surfaces. For convenience, the surface energies and phase diagrams were plotted using  $\Delta\mu = \mu - \mu^*$ . For  $\mu^*(A)$  we used metallic Li or Na. For  $\mu^*(O)$  the reference state corresponds to one half of the O<sub>2</sub> energy in the cell at 0 K. Since the PBE functional overestimates the binding energy of O<sub>2</sub>-molecule, we corrected it by 1.36 eV, as estimated by Wang et al. [41].

For a cathode material inside a Li(Na)-ion cell with the metallic Li (Na) anode, the  $\Delta\mu(A)$  is connected to the open circuit voltage ( $V = -\Delta\mu(A)/e$ ) [27,42,43] keeping in mind that the calculated value of  $\Delta\mu(A)$  is approximated by the change in internal energy at 0 K [42].

Phase diagrams were constructed using a grand canonical potential phase diagram module [44,45] as implemented in the pymatgen package [46]. The list of stable phases for (Li/Na) – (Co/Ni) – O systems were taken from the Materials Project [37].

For modeling surface reconstructions, we used an in-house Monte-Carlo (MC) code, which is also integrated into the SIMAN package [34]. In the developed code different atomic structures are generated by a random swapping of  $M$ ,  $A$ , and vacancies (e.g. from the surface) followed by atomic optimization and total energy calculation by DFT+U. At each MC step, the Metropolis criterion is applied for acceptance of the configuration depending on the chosen temperature. The accepted configuration is used for further generation of defects. The increased temperature allows overcoming activation barriers for reconstruction. We performed MC simulation at 0 K and 1100 K, which is a typical annealing temperature for the layered oxides. For the largest considered slab with 924 possible configurations up to 50 consecutive MC steps were applied. By performing several separate runs this was shown to be enough to find the lowest energy configuration.

The slab for the MC calculations was divided into three parts: the surface with a few layers where swapping and optimization are allowed, an intermediate part where only optimization is allowed and a frozen part which mimics the bulk material. To speed up the calculation, the code ignores those swaps where coordination of transition metals is reduced, as they are assumed to be unfavorable.

## 3. Electronic and crystal structure of layered oxides

### 3.1. Chosen oxides and their crystal structure

We consider four pure oxides: LiNiO<sub>2</sub>, LiCoO<sub>2</sub>, NaNiO<sub>2</sub>, and NaCoO<sub>2</sub>. To select the relevant crystal structure, we rely on battery-related experimental and computational literature data.

For LiNiO<sub>2</sub> the experimentally reported crystal structure is  $R\bar{3}m$  [47]. However, a recent DFT/DFT+U study showed that the most stable crystal structure of LiNiO<sub>2</sub> at 0 K obtained with this method is  $P2/c$  with Ni<sup>2+</sup>/Ni<sup>4+</sup> charge ordering [48]. Our calculations confirmed that  $P2/c$  is more stable than the  $R\bar{3}m$  structure and Jahn–Teller distorted  $P2_1/c$  structure by 14 meV/atom and 0.1 meV/atom, respectively. While the  $P2/c$  structure was not confirmed experimentally, it shows robust electronic and ionic convergence and was adopted in this study. On the contrary, relaxation of ASC in a supercell with the  $R\bar{3}m$  structure causes partial JT distortions preventing correct extraction of

formation energies with respect to ideal  $R\bar{3}m$ . Overall, due to the small energy difference per atom between  $\text{LiNiO}_2$  phases, their choice should have little impact on antisite formation energies if the same phases are used in two compared supercells.

To construct bulk supercells, we use the  $P2/c$  crystal structure directly. To construct slabs we use the  $R\bar{3}m$  primitive cell, with further structural optimization allowing charge-disproportionation and careful control of the obtained orbital and magnetic structure. For  $\text{LiCoO}_2$  no charge ordering or Jahn–Teller distortion was observed and the main electrochemically active phase is  $R\bar{3}m$  [49,50], which we also adopt in our study.

For  $\text{NaNiO}_2$  two electrochemically active phases are  $C2/m$  (low temperature phases) [51,52] and  $R\bar{3}m$  (high temperature phase) [53]. In our calculations, we use only the  $C2/m$  crystal structure. For  $\text{NaCoO}_2$  [54] the electrochemically active phases are  $R\bar{3}m$  [55,56] and  $P6_3/mmc$  [57,58]. Both phases are usually stabilized with Na deficiency, which is especially pronounced for  $P6_3/mmc$ , though  $\text{NaCoO}_2$  stoichiometry can be also achieved for  $R\bar{3}m$  phase [59].

For bulk calculations we consider both  $R\bar{3}m$  and  $P6_3/mmc$  crystal structures, while for slabs we limit ourselves to the  $R\bar{3}m$  phase.

### 3.2. Lattice constants and electronic structure

The calculated lattice constants for  $\text{AMO}_2$  ( $A = \text{Li, Na, } M = \text{Ni, Co}$ ) in comparison to experiment and other calculations are summarized in Table S1. Our values overestimate the experimental values by 0.7%, 0.9%, 0.7% and 0.4% for  $\text{LiNiO}_2$ ,  $\text{LiCoO}_2$ ,  $\text{NaNiO}_2$ , and  $\text{NaCoO}_2$ , respectively. The  $\text{NaNiO}_2$  is additionally characterized by a Jahn–Teller distortion with four short (1.91 Å) and two long (2.19 Å) Ni–O bonds.

The PDOS for  $\text{AMO}_2$  are provided in Figs. S1–S2. The calculated band gaps for  $\text{LiCoO}_2$ ,  $\text{NaNiO}_2$ , and  $\text{NaCoO}_2$  are 2.2, 0.2, and 2.1 eV, respectively. The metastable  $\text{LiNiO}_2$  in the  $R\bar{3}m$  space group has metallic states at the Fermi level, while in  $P2/c$  a band gap of 0.6 eV appears.

In Li and Na based oxides Co is in the low-spin state [60] with the magnetic moment of zero, corresponding to a formal oxidation state of  $\text{Co}^{3+}$ . In  $\text{LiNiO}_2$  ( $P2/c$ )  $\text{Ni}^{2+}$  and  $\text{Ni}^{4+}$  have  $1.77 \mu_B$  (HS) and  $0.11 \mu_B$  (LS) magnetic moments, respectively. In  $\text{NaNiO}_2$  the magnetic moment of Ni is  $1.17 \mu_B$ , which is close to a LS state of  $\text{Ni}^{3+}$ . These magnetic moments are consistent with literature values [48].

## 4. Surface energies of ideal terminations

### 4.1. Determination of equilibrium surfaces

To determine equilibrium surfaces we adopt the same approach as was proposed by Kramer et al. [20]. In the first step, we build a phase diagram in chemical potential space, which allows for determination of the stability windows of the phases of interest. The obtained chemical potentials allow calculating surface energies for non-stoichiometric surfaces according to Eq. (1), which is followed by the construction of crystal Wulff shapes and identification of most relevant surfaces depending on the synthetic conditions. The calculated phase diagrams and corresponding chemical potential regions are shown in Fig. S3 and Table S2, respectively.

### 4.2. Surface energies of ideal surfaces

The list of considered surfaces is taken from the literature, which includes non-polar, polar, stoichiometric, and non-stoichiometric cases [19,20,26]. While it is always possible to include more surfaces, it was shown by Kramer et al. that in  $\text{LiCoO}_2$ , surfaces with large Miller indices are of less importance [20], which should be valid for other layered oxides as well.

The calculated surface energies as a function of chemical potential are plotted in Fig. 1. The plot allows for identifying the most stable

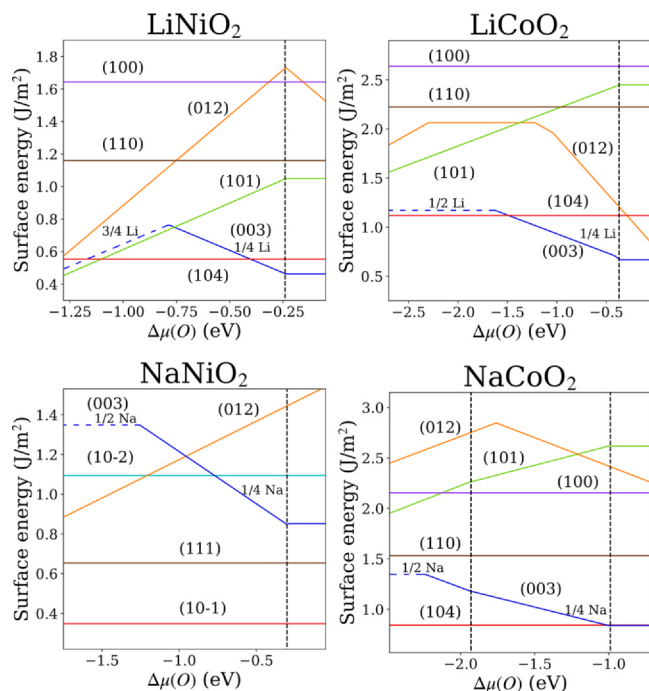


**Fig. 1.** DFT+U surface energies depending on chemical potential calculated with Eq. (1) phase diagrams shown in Fig. S3. For (003), (012) and (101) surfaces the configurations with 0, 1/4, 1/2, 3/4, and 1 Li/Na monolayer are considered. The vertical line denotes change of enclosing phase o.n phase diagram.

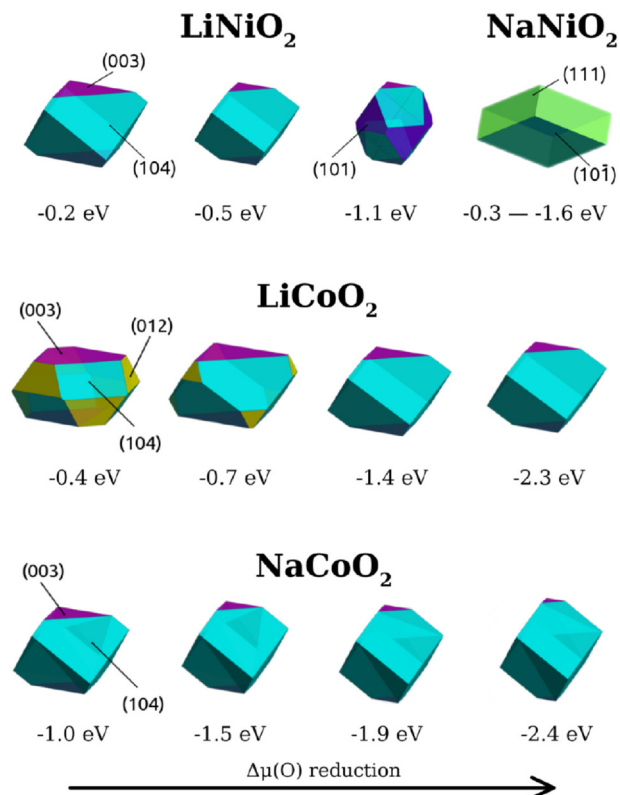


**Fig. 2.** Equilibrium shapes of  $\text{LiNiO}_2$ ,  $\text{LiCoO}_2$ ,  $\text{NaNiO}_2$  and  $\text{NaCoO}_2$  at different values of  $\Delta\mu(\text{O})$ .

surfaces for each value of oxygen chemical potential. Using this information we construct Wulff shapes for representative values of oxygen chemical potentials, which are collected in Fig. 2.

**Table 1**

Calculated surface energies ( $\text{J}/\text{m}^2$ ) for stoichiometric non-polar and polar surfaces in  $\text{AMO}_2$ . The surface energies of  $\text{LiNiO}_2$  are calculated with respect to the  $\text{LiNiO}_2$  ( $P2/c$ ) bulk phase. For (003) the values are provided for a 1/2 monolayer of Li/Na. For monoclinic phase the  $(10-1)_m$  and  $(111)_m$  both corresponds to  $(104)_{\text{hex}}$ . The  $(001)_m$  surface corresponds to  $(003)_{\text{hex}}$ .

Oxide	Structure	Facet	Our	Liang [26]	Cho [19]	Kramer [20]
$\text{LiNiO}_2$	$R\bar{3}m$	(104)	0.70	0.53	0.64	
		(003)	0.90	0.71	0.97	
		(110)	1.25	1.22	1.24	
		(100)	1.75	1.80	1.65	
$\text{LiCoO}_2$	$R\bar{3}m$	(104)	1.12			1.05
		(003)	1.17			1.04
		(110)	2.22			2.24
		(100)	2.64			2.94
$\text{NaNiO}_2$	$C2/m$	(10 $\bar{1}$ )	0.35			
		(111)	0.65			
		(001)	1.35			
		(110)	1.53			
		(104)	1.85			
		(100)	1.01			
		(10 $\bar{2}$ )	1.09			
$\text{NaCoO}_2$	$R\bar{3}m$	(104)	0.84			
		(003)	1.35			
		(110)	1.53			
		(100)	2.37			

For Li based oxides the Wulff shape and corresponding morphology of particle show noticeable dependence on the oxygen chemical potential. For  $\text{LiNiO}_2$  with the lowering of  $\Delta\mu(\text{O})$  the contribution of the (104) surface is reduced, while the contribution of  $(10\bar{1})$  is increased. In contrast, for  $\text{LiCoO}_2$  the contribution of (104) surface is increased, while the contribution of (012) is reduced.

For Na based oxides, changes of the Wulff shape are less pronounced. In the case of  $\text{NaNiO}_2$ , the Wulff shape is fully determined by two stoichiometric surfaces, (111) and  $(10\bar{1})$ , and has no dependence on chemical potential. In the case of  $\text{NaCoO}_2$  a slow reduction of the (003) surface contribution is observed along with  $\Delta\mu(\text{O})$  lowering.

Overall, inside  $\text{AMO}_2$  stability windows, the contribution of the non-stoichiometric surfaces is minor in Li-based oxides and absent in Na-based oxides. The energies for stoichiometric surfaces are collected in Table 1.

For the rhombohedral phases, the non-polar (104) surface shows the lowest energy of all the oxides. It is lower by 10% than the next lowest energy surface (003), which is polar. The low energy of (104) is fortunate as this surface is highly attractive for Li extraction through it, while the (003) surface does not allow Li extraction. The atomic structure of these surfaces obtained after relaxation is shown in Fig. 3 on the example of  $\text{LiNiO}_2$ . For the monoclinic  $\text{NaNiO}_2$  phase, the lowest energy surfaces are  $(10\bar{1})_m$  and  $(111)_m$ . The two surfaces are inherited from  $(104)_{\text{hex}}$  due to symmetry splitting. The  $(001)_m$  surface, which corresponds to  $(003)_{\text{hex}}$  has much larger energy than  $(111)_m$ . Therefore,  $\text{NaNiO}_2$  has the optimal Wulff shape from the electrochemical point of view as both  $(10\bar{1})_m$  and  $(111)_m$  expose Na channels. Additional explanations of these surface energetics are provided in the Discussion Section 6.1.

The agreement with available literature data for Li-based oxides is good, though our values for  $\text{LiNiO}_2$  are somewhat larger than that of Cho et al. [19] and Liang et al. [26]. The reason for that is related to the fact that we used the  $P2/c$  bulk phase as a reference, which is more stable than  $R\bar{3}m$  [48]. The energy of (104) is lower than 1/2(003) by  $0.2 \text{ J}/\text{m}^2$ , which is in agreement with Liang et al. The larger difference of  $0.3 \text{ J}/\text{m}^2$  obtained by Cho et al. seems due to their overestimated energy of 1/2(003) surface, which we found difficult to converge. In particular, we were able to find the lowest energy magnetic

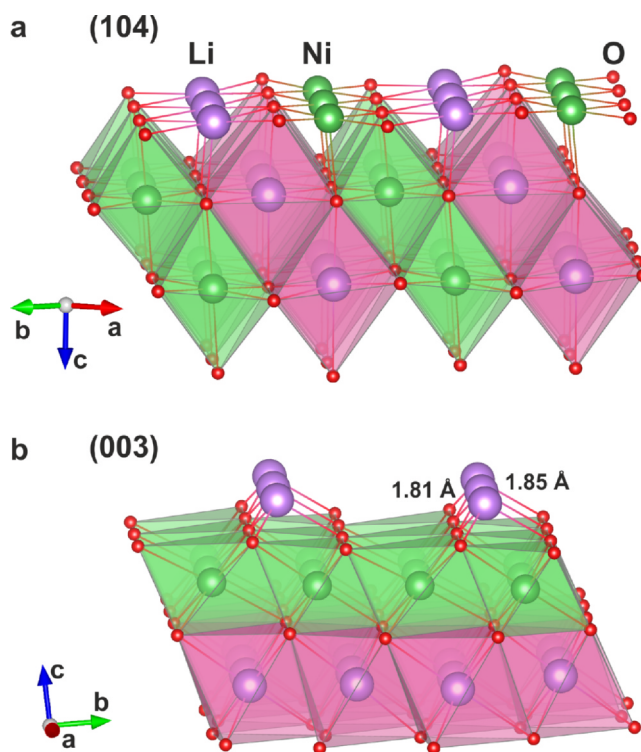


Fig. 3. The atomic structure of the (104) and (003) surfaces in  $\text{LiNiO}_2$ .

configuration of 1/2(003) only with the help of the U-ramping method [61] and Monte Carlo sampling of surface magnetic configurations. The obtained magnetic structures used for antisite defect calculations are described in the next section.

#### 4.3. Magnetic and electronic structure of selected surfaces

In the (104) surface of  $\text{LiNiO}_2$ , the magnetic structure (Fig. S4) is slightly different from that in bulk, however, charge disproportionation is still observed. The surface Ni is more close to  $\text{Ni}^{2+}$  with a magnetic moment of  $1.41 \mu_B$ , while the subsurface layer is characterized with slightly oxidized Ni with a magnetic moment of  $1.04 \mu_B$ , while the next layer is slightly reduced ( $1.6 \mu_B$ ) and then again oxidized. The PDOS for Ni in bulk  $P2/c$  and (104) slab are shown in Fig. S2 and Fig. S5, respectively. Indeed, the PDOS of surface Ni resembles that of the bulk  $\text{Ni}^{2+}$ , though the PDOS of subsurface Ni is different from bulk  $\text{Ni}^{4+}$ . In turn, this Ni is closer to Jahn–Teller distorted Ni in the  $\text{LiNiO}_2$  phase with the  $P2_1/c$  space group. Since this structure is only by 0.1 meV/atom higher in energy the influence on surface energies should be minor due to this inconsistency [48]. For the (003) surface of  $\text{LiNiO}_2$  the surface Ni layer shows a strong disproportionation to  $\text{Ni}^{2+}$  ( $1.77 \mu_B$ ) and  $\text{Ni}^{4+}$  ( $0.07 \mu_B$ ), while the internal layers are characterized with intermediate magnetic moments ( $1.2 \mu_B$ ) and Jahn–Teller distortions as in the previous case.

For the (104) surface of  $\text{LiCoO}_2$ , the optimization shows that the system ends up in several magnetic configurations with either all surface atoms in a LS state or intermediate spin (IS)/LS combinations, where IS can have a magnetic moment of 2 or  $3 \mu_B$ . Such mixed configurations show slightly lower energies, which was also found earlier in computational studies [62]. However, in the IS case the two surfaces of the slab have different magnetic ordering, despite starting from fully symmetric distortions and magnetic moments. Therefore, when considering surface antisites we adopt the LS configuration, since it is more reliable in terms of self-consistent field convergence.

The PDOS on the (104) surface Co (5-coordinated) in LS and IS states are provided in Fig. S8, where Co in IS state has a small density of

states at Fermi level. For (003) the most stable found configuration is characterized by surface Co in the low spin state with zero magnetic moments.

In NaCoO<sub>2</sub> slabs, all Co atoms are steadily converge in a low-spin state with zero magnetic moments, though slightly lower energy configurations with IS states can be also obtained. In NaNiO<sub>2</sub>, surface Ni has an orbital structure similar to that in bulk with surface magnetic moments of 1.18  $\mu_B$  (1.17  $\mu_B$  in the bulk).

## 5. Bulk and surface antisite defects

### 5.1. Bulk antisite defect pairs

Before coming to surface defects we first consider bulk stoichiometric antisite defect pairs, which can be produced by a simple swapping of  $M$  and  $A$  cations. In this paper, by antisite defect complex (ASC) we mean a complex of  $M_A$  and  $A_M$  components and an additional small hole polaron, which can form due to the charge disproportionation effect. The choice of stoichiometric defects is driven by the fact that DFT+U provides better results for such cases [63]. Also, their formation energies do not depend on chemical potential, which simplifies reproduction and comparison of results. The calculated formation energies of ASC for considered layered oxides are collected in Table 2 for three separations between  $M_M$  and  $A_A$  sites (denoted 1 NN, 2 NN, and 3 NN). The atomic structure of antisite complexes for 1 NN and 2 NN separations are shown in Fig. 4 on the example of LiCoO<sub>2</sub>. For Li-based oxides, a very small difference between 1 NN and 2 NN configurations, and increase at 3 NN are observed, showing that the antisite components attract each other. For Na-based oxides the lowest energy configuration is 2 NN. The reasons for such behavior are explained in the Discussion Section 6.4.

We find that in all cases after optimization the formal oxidation state (orbital order) of  $M$  in the  $A$  site is + 2, which is confirmed by the magnetic moments, PDOS and charge density. For those cases, where  $M$  was originally in the + 3 state (LiCoO<sub>2</sub>, NaCoO<sub>2</sub>, and NaNiO<sub>2</sub>) one neighboring  $M$  cation can be additionally oxidized to the + 4 state, which is easily detected by reduction of  $M$ -O bonds and a change of

**Table 2**

DFT+U calculated formation energies of antisite defects in layered oxides for three smallest  $M_A - A_M$  separations in comparison with literature data. The values for the most favorable small polaron configuration described in the text are provided. NN – nearest neighbor.

Oxide	NN	$M_A - A_M$ , Å	Our $E_f$ , eV	Other $E_f$ , eV
LiNiO <sub>2</sub>				
$P2/c$	1nn	2.86	0.65	0.75 [23]
	2nn	4.08	0.62	
	3nn	4.96	0.77	
LiCoO <sub>2</sub>				
$R\bar{3}m$	1nn	2.82	1.80	2.34 [22], 1.4 [23]
	2nn	4.07	1.80	
	3nn	4.92	2.05	
NaNiO <sub>2</sub>				
$C2/m$	1nn	3.10	2.40	2.4 [23]
	2nn	4.22	2.07	
	3nn	4.53	2.41	
NaCoO <sub>2</sub>				
$R\bar{3}m$	1nn	2.94	3.16	
	2nn	4.22	2.90	
	3nn	5.12	4.30	
$P6_3/mmc$	1nn	2.94	3.34	
	2nn	4.22	3.10	
	3nn	5.12	4.50	

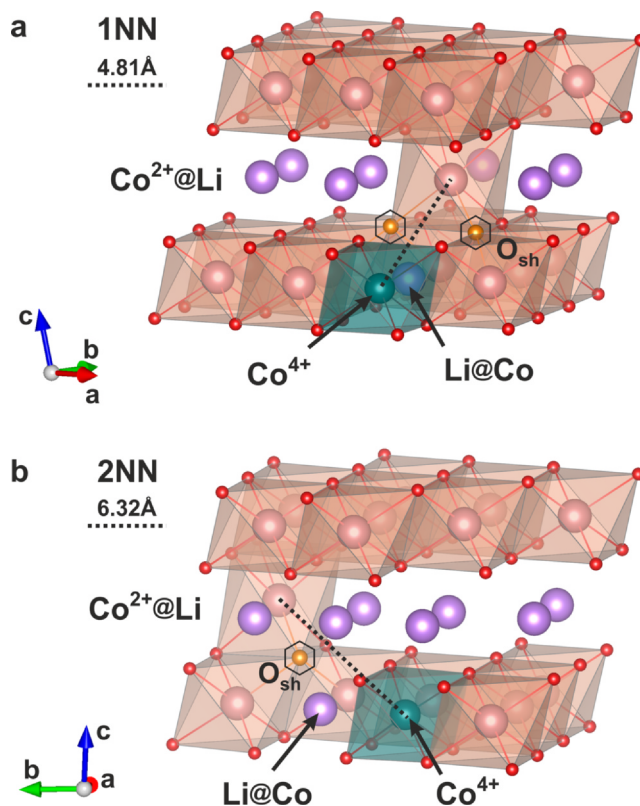


**Fig. 4.** The atomic structure of 1 NN and 2 NN antisite complexes in LiCoO<sub>2</sub>. The distance is provided between Co<sub>Li</sub> and Co<sub>Co</sub> (AP).

magnetic moment. Further in the text we call this defect an additional small hole polaron (AP). Hence, the exchange of  $A$  and  $M^{3+}$  results in a complex defect which consists of three components:  $M'_A$ ,  $A''_M$ , and  $A(M'_M)$  (see Fig. 4). A similar result was obtained by Hoang et al. for Jahn-Teller distorted LiNiO<sub>2</sub> and NaNiO<sub>2</sub> using hybrid functional HSE06 [22]. In the case of LiNiO<sub>2</sub> ( $P2/c$ ), where half of the Ni is present in a + 2 state, exchange with Li does not change its orbital order (the PDOS on Ni<sub>Li</sub> is very similar to that of Ni<sup>2+</sup> in bulk though shifted to lower energies due to increased Li-O distances, see Fig. S9) and does not produce any AP.

To find the most favorable position of AP we have prepared different initial configurations by localizing small hole polaron on several symmetrically non-equivalent  $M$  sites by a local decrease of  $M$ -O bonds (by 0.2 Å). After optimization, the location of AP was identified from magnetic moments. The final position of an AP does not always coincide with the initial local deformation but can be either localized at some other  $M$  site or end up in the delocalized state. The lowest energy configurations are those when an AP is localized on the first NN d-metal position from  $A_M$ , and at least on the third NN d-metal from  $M_A$ . The reasons for that are provided in the Discussion 6.5 section. Other configurations, where an AP is localized on the first or second NN from the  $M_A$  or fully delocalized states can be 0.4 eV higher in energy.

For LiCoO<sub>2</sub> and NaCoO<sub>2</sub> the localized AP is the most stable state, while for NaNiO<sub>2</sub> the delocalized state is slightly lower in energy (by 0.05–0.1 eV). The values provided in Table 2 correspond to the lowest energy configurations.

### 5.2. Surface and subsurface antisite defect pairs

The surface antisite defect pairs are calculated for (104)<sub>hex</sub>/(10–1)<sub>m</sub> surface, which is the most relevant from the electrochemical point of view. To reduce the interaction between defect images the surface area of slab was chosen to 3 × 2 (8.5 Å by 11.5 Å for LiCoO<sub>2</sub>).

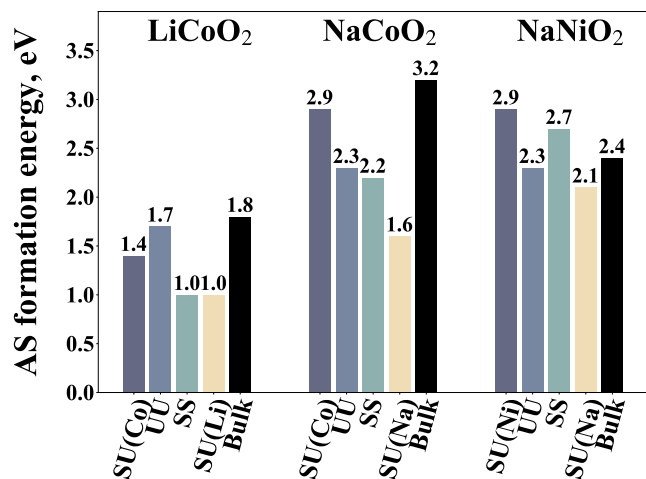


Fig. 5. DFT+U calculated surface ASC formation energies (eV) on (104) surface for 1NN in comparison with bulk results. The values for the most favorable small polaron configuration described in the text are provided. SS is ASC in surface layer, SU is ASC between surface and subsurface layers, element in parenthesis specify surface element, UU is ASC in subsurface layer.

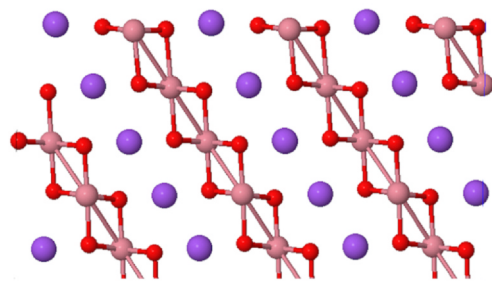
Due to the significant complexity of the magnetic structures here we omit LiNiO<sub>2</sub>, while for other cases special measures are taken to localize the small polarons by providing initial local deformations. The ASC formation energies are provided only for those cases, where magnetic structures of the slab with ASC defect and ideal slab fully correspond to each other except for changes caused by ASC defect itself.

We create 1 NN surface-surface (SS), surface–subsurface (SU), and subsurface–subsurface (UU) ASC configurations. Due to the rearrangement of surface atoms, two possibilities with slightly shorter and slightly longer separations between antisite components are available for SS and UU. Both possibilities are calculated and it turns out that shorter separations have lower energies, which are collected in Fig. 5 and Table S3. Overall, the surface ASC energies are lower than their bulk analogs, which is especially pronounced in the case of Co-based oxides.

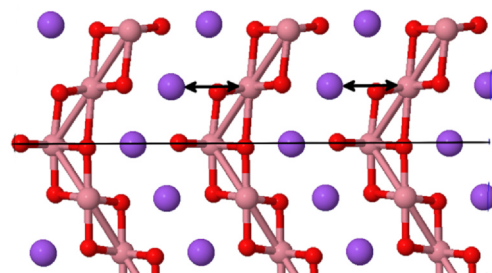
In LiCoO<sub>2</sub> the SS configuration is by 0.8 eV lower than that in the bulk, reducing to just 1 eV. A similar energy is obtained for the SU configuration with Li on the surface. The formation of a SU ASC with Co on the surface requires 1.4 eV, which highlights the higher TM–O bond breaking energy compared to the A–O bond. The formation energy of UU ASC is only 0.1 eV lower than that of bulk. A more pronounced reduction is observed in NaCoO<sub>2</sub>, where SS and SU (Na) are reduced from 3.2 eV to 2.2 and 1.6 eV, respectively. Interestingly, a noticeable reduction of ASC formation energy is observed for UU (from 3.2 to 2.3 eV). In NaNiO<sub>2</sub> the reduction of surface ASC energy is much less pronounced with SU (Na) being the most stable configuration (2.1 vs 2.4 eV in bulk).

Regarding the magnetic configuration of surface ASC, the same trend as in the bulk case is observed. The *M* at the *A* site is always in a high-spin + 2 state with the formation of AP on one of the available *M* sites (+ 4 state). As in the bulk case, an AP prefers to be at 1 NN from *A<sub>M</sub>* and at least at 3 NN from *M<sub>A</sub>* component. Interestingly, the AP in the case of surface ASC prefers to be localized not only in Co-based oxides but also in some NaNiO<sub>2</sub> cases, though the most stable configuration still corresponds to a delocalized state. The additional complication is related to the fact that AP can localize either at the surface or at subsurface layers, which is additionally specified in Table S3. In Co-based oxides, the lowest ASC formation energies correspond to surface localization of AP. This can be related to the easier relaxation of small polarons at the surface.

### a) Ideal (104) surface



### b) Twin formation



### c) Blocking reconstruction

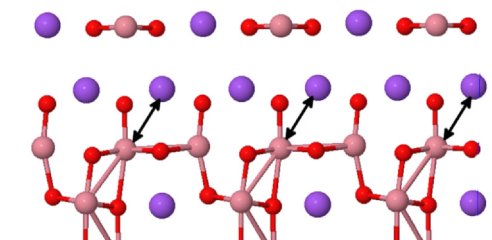


Fig. 6. Representative surface structures obtained after Monte Carlo and atomic optimization on the example of slab with (104) surface in *R3m* crystal structure: ideal, twin, and blocking reconstruction. A atoms are purple, M atoms are pink, and O atoms are red.

### 5.3. Surface reconstruction

Surface reconstruction can include a change of stoichiometry, a shift of oxygen layers, and the formation of ASC defects. Here we focus only on reconstruction with fixed stoichiometry caused by the formation of antisite defect pairs to be compared with individual surface antisites. To take into account the formation of several ASCs and find their most favorable configuration we use a Monte-Carlo algorithm described in Section 2. As in the previous section we consider only (104)<sub>hex</sub>/(101)<sub>m</sub> surface, however taking the 1 × 1 and 2 × 1 surface areas and including LiNiO<sub>2</sub>.

Our Monte Carlo simulation shows that two representative surface configurations can be obtained using the 1x1 supercell (Fig. 6). The first configuration corresponds to the formation of one SU ASC defect, which results in a full rearrangement of the (104) layers. In particular, the U and U2 layers contain only *A* and *M* atoms, respectively (Fig. 6 (c)). However, it turns out, that the formation energy per one ASC in this kind of blocking reconstruction is slightly higher than that for an individual SU ASC. Therefore, we conclude that no additional driving force exists for reconstruction, which can be caused by ASC interactions with each other. The second configuration is generated due to the formation of two successive ASC defects, which is equivalent to

subsurface twin boundary with a low energy of 0.1 J/m<sup>2</sup> (Fig. 6 (b)).

## 6. Discussion

### 6.1. Influence of termination and composition on surface energies

To explain the order of surface energies we recall two well-established rules. Firstly, the surface energy correlates with the number of broken *M*–O bonds [64,20]. Secondly, polar surfaces are usually higher in energy than their non-polar counterparts due to polarity compensation mechanism [65].

The first rule explains Li or Na termination of the lowest energy polar surface (003). Though in the general case, the concentration of alkali atoms depends on the  $\mu(\text{O})$ , for further comparisons we use a special case of (003) with 1/2 of Li or Na on the surface. Due to the symmetrical stoichiometric slab, such a surface has no dependence on chemical potential.

The second rule explains the lower energy of (104) surface compared to 1/2(003). The (104) surface, despite breaking 0.12 *M*–O bonds per Å<sup>2</sup>, is non-polar with almost ideally neutral layers and minor disturbance of the lattice. For example in LiCoO<sub>2</sub> the average Li–O distance at the (104) surface remains very close to that in the bulk (2.1 Å), while at the (003) surface it quite noticeably reduces to 1.8–1.9 Å (see Fig. S10, Table S4 and Table S5).

The comparison of LiCoO<sub>2</sub> and NaCoO<sub>2</sub> shows that the energy of the 1/2(003) surface is larger by 0.2 J/m<sup>2</sup>, while the energy of (104) is smaller by 0.3 J/m<sup>2</sup> for Na. The increase of the (003) energy is related to the increase of Na–O distance and the corresponding enhancement of polarity compensation. The reduction of the (104) energy is affected by weaker bonds in Na-based oxide than in Li-based oxides, reducing the bond-cutting contribution to the surface energy.

Comparison of LiNiO<sub>2</sub> and NaNiO<sub>2</sub> shows the same trend. The energy of 1/2(001)<sub>*m*</sub> (analogue of 1/2(003)<sub>*hex*</sub>) is increasing by 0.45 J/m<sup>2</sup>, while the energy of (101)<sub>*m*</sub> (analogue of (104)<sub>*hex*</sub>) is reducing by 0.35 J/m<sup>2</sup>. However, in this case, an additional complication is caused by a monoclinic distortion. The (104)<sub>*m*</sub> is splitting into {10–1}<sub>*m*</sub> and {111}<sub>*m*</sub> families with the latter having a 0.3 J/m<sup>2</sup> higher energy.

Overall, the surface energies of Co-based oxides are higher than that of Ni-based both for Li and Na, which is explained by stronger Co–O bonds [66].

### 6.2. Electronic structure of ASC

In the previous sections, we proposed that *M<sub>A</sub>* is in a + 2 oxidation state. Such a conclusion is obtained from *M*–O bond lengths and magnetic moments, which are 1.78, 2.67, 1.76, and 2.66 μ<sub>*B*</sub> for Ni<sub>*Li*</sub>, Co<sub>*Li*</sub>, Ni<sub>*Na*</sub>, and Co<sub>*Na*</sub>, respectively. These magnetic moments are consistent with the high spin–orbital order of corresponding elements. However, it should be noted that the notion of the oxidation state here is rather formal. In particular, analysis of charge density shows that the real change of charge on Co or Ni in *A* site compared to their original sites is much less than one. The same is true for *M* with AP, where the formal oxidation state is + 4 (low spin, 0.9 μ<sub>*B*</sub> for Co and 0.2 μ<sub>*B*</sub> for Ni), but the change of charge is also much smaller than one. Such behavior of late transition metals in oxides is well known. In particular, Aydinol et al. showed with DFT calculations that oxidation of Co during Li extraction from LiCoO<sub>2</sub> has a small influence on total charge of Co rather causes redistribution between *t<sub>2g</sub>* and *e<sub>g</sub>* orbitals [42].

The difference between formal oxidation states is well seen from PDOS, which are shown for Co in three oxidation states in Figs. S6 and S7. Comparison of Co<sub>*Co*</sub><sup>x</sup> and Co<sub>*Li*</sub> shows the following changes: (i) transfer of *d* DOS from the empty to the filled states (disappear of spin up peak between 2 and 3 eV and increase of spin up *d* density below Fermi energy); (ii) reduction of *p* DOS; (iii) more uniform distribution of DOS in –7.0 energy range. These redistributions are in line with the change of electronic state from *t<sub>2g</sub><sup>6</sup>e<sub>g</sub><sup>0</sup>* to *t<sub>2g</sub><sup>5</sup>e<sub>g</sub><sup>2</sup>*.

### 6.3. Influence of transition and alkali metal on ASC energy

One of the reasons for the larger antisite pair energy in LiCoO<sub>2</sub> compared to LiNiO<sub>2</sub> is related with unfavorable charge disproportionation of Co<sup>3+</sup> to Co<sup>2+</sup> (*M<sub>A</sub>*) and Co<sup>4+</sup> (AP), which is absent in LiNiO<sub>2</sub> (*P2/c*). Indeed, our calculations show that the exchange of Ni<sup>4+</sup> and Li<sup>+</sup> results in a charge redistribution and ASC energy of 1.2 eV, compared to 0.65 eV for Ni<sup>2+</sup>–Li exchange. This explanation is relying on the charge-ordered (*P2/c*) structure, which we adopted in our study. However, in Jahn–Teller LiNiO<sub>2</sub> with only Ni<sup>3+</sup> the charge disproportionation should be easier than in LiCoO<sub>2</sub>.

Another reason is usually attributed to the mismatch of cationic radii, which is somewhat contradictory. The comparison of Li<sup>+</sup>/Co<sup>3+</sup> (LS) (0.76 Å/0.545 Å) and Li<sup>+</sup>/Ni<sup>3+</sup> (LS) (0.76 Å/0.56 Å) ratios shows that Li is almost equally squeezed both in the Co and Ni sites (here we use Shannon definition for ionic radii [67]). Assuming though the existence of larger Ni<sup>2+</sup> (0.69 Å), as in the *P2/c* phase, makes it more suitable for Li. The comparison of Co<sup>2+</sup>/Li<sup>+</sup> (0.745 Å/0.76 Å) and Ni<sup>2+</sup>/Li<sup>+</sup> (0.69 Å/0.76 Å) ratios shows that in this case Co fits much better to the Li site. Taking into account, that *M*–O bonds are stronger than *A*–O, ideal matching of Co<sup>2+</sup> should be more important in reducing the ASC energy in LiCoO<sub>2</sub> that makes ionic size arguments controversial. One more reason that is responsible for the reduction of the ASC energy in LiNiO<sub>2</sub> is proposed in the literature and related to the Ni–O–Ni super-exchange interaction, which seems more profound compared to the ionic size arguments [23,68].

While the influence of *M* on the ASC formation energy is somewhat complicated due to different contributions, the influence of the alkali metal can be explained by the ionic mismatch arguments. Due to a noticeably larger ionic size of Na<sup>+</sup> (1.02 Å), the Na<sub>*M*</sub> is squeezed as compared to Li<sub>*M*</sub>. For example, the Na<sub>*Ni*</sub>–O and Na<sub>*Co*</sub>–O distances increase after relaxation by 8.6 and 9.9%, respectively, while for Li these distances increase only by 0.6 and 5%. The opposite is true for *M<sub>Na</sub>*, which is much looser compared to *M<sub>Li</sub>*.

### 6.4. Energy difference between 1 NN and 2 NN ASC configurations

The 1 NN and 2 NN configurations are similar in a sense that in both cases *M<sub>A</sub>* and *M<sub>M</sub>* components share common oxygen atoms (*O<sub>sh</sub>*): two *O<sub>sh</sub>* in 1 NN and one *O<sub>sh</sub>* in 2 NN (Fig. 4). These shared oxygens can be responsible for additional ASC stabilization compared to other configurations with larger separations. Indeed, the sharing of oxygen atoms allows a simultaneous contraction of the *M<sub>A</sub>*O<sub>6</sub> and an expansion of *M<sub>M</sub>*O<sub>6</sub> octahedra with less distortion of the surrounding lattice as one or two shared oxygens are simply shifting towards *M<sub>A</sub>*. We obtained that in 1 NN the shift of two *O<sub>sh</sub>* towards *M<sub>A</sub>* is accompanied by the increase of the distance between these oxygens (*d<sub>O–O</sub>*) from 2.85 to 2.97 Å (in LiCoO<sub>2</sub>). In the 2 NN configuration the *O<sub>sh</sub>* simply shifts to *M<sub>A</sub>* along the line connecting *M<sub>A</sub>* and *M<sub>M</sub>*.

As for the energy difference between 1 NN and 2 NN, it is negligible in Li-based oxides but quite pronounced in the Na-based oxides, where 2 NN configuration is by 0.3 eV more stable than 1 NN. This is caused by a larger ionic mismatch and more pronounced *O<sub>sh</sub>* shifts. In the 1 NN configuration the shift of *O<sub>sh</sub>* causes a strong contraction of two *O<sub>sh</sub>*–Na<sub>*Na*</sub> bonds from 2.31 Å to 2.17 Å, penalizing the energy of the ASC formation. In 2 NN though, the *O<sub>sh</sub>*–Na<sub>*Na*</sub> bond is only slightly increasing, implying no additional energy penalty.

### 6.5. Stable AP positions

The localization of AP (*M<sup>4+</sup>*) at specific positions in Co-based oxides is also explained by the sharing of oxygen atoms with other ASC components. The contracted *M<sup>4+</sup>*O<sub>6</sub> octahedron prefers to share oxygen with the expanded *M<sub>M</sub>*O<sub>6</sub> octahedron and avoids neighboring with contracted *M<sub>A</sub>*O<sub>6</sub>. As a result of that, the most stable AP position is the first nearest neighbor d-metal from *M<sub>M</sub>* and third nearest neighbor d-

metal from  $M_A$ . We found that by preparing such input deformations the system steadily and quickly converges as the lowest energy configuration.

### 6.6. Surface ASC and reconstruction

The surface ASC defect is similar to that in bulk in two ways: the HS + 2 state of  $M_A$  and + 4 state of AP, the position of which is also governed by the factors related to the shared oxygens. At the same time, the presence of a surface introduces several new structural variants of ASC that have a noticeable influence on the energetics.

Firstly, a surface – surface ASC can have a lower formation energy due to the easier relaxation of both  $M_A$  and  $A_M$  components with the reduced coordination. Secondly, the surface–subsurface ASC with  $A$  at the surface is additionally stabilized by the reduced number of broken  $M$ –O bonds. The surface ASC energetics can be additionally affected by the magnetic configuration of the surface. In particular, as was mentioned in Section 4 for Co-based oxides the presence of HS Co at the surface can reduce its energy. Therefore, checking its influence on the ASC formation energies is of further interest, while it was skipped in the current study due to considerably increasing complexity.

Overall, the easier formation of ASC on the surface predicted by DFT is in line with experimental observations of surface reconstruction. In particular, the ASC defects formed during cycling in the bulk of material can migrate to the surface enhancing reconstruction. At the same time, the surface ASC remains unstable defect with a relatively large formation energy (~1 eV) leaving unclear the origin of surface reconstruction in pristine particles observed in several experimental studies. One explanation can be related to the influence of alloying elements and complex compositions used in these works. Therefore, the experimental study of reconstruction in simple systems can shed more light. On the other hand, more variants of surface reconstruction such as the shift of  $MO_6$  sheets and rock-salt transformations with the change of surface chemical composition should be considered computationally. For example it was shown experimentally that the surface composition of  $LiNiO_2$  resembles those of  $NiO$  [69]. Another interesting aspect is the influence of electrolyte and solid/liquid interface on the surface structure and ASC defects, which can be also taken into account computationally using polarizable continuum models. For example, a recent computational study shows that for  $LiCoO_2$  up to 16% of surface Co undergo dissolution in water [70].

To resolve raised questions it may require to consider formation of individual charged antisites at the surface analogous to the computational approach used by Hoang et al. for the bulk case [22]. Hoang et al. showed that at reducing environment the most stable defect in  $LiCoO_2$  is  $Co_{Li}^+$  with the formation energy of 0.55 eV, which is comparable with the reduction of the surface ASC energy, obtained in our study. Assuming that the reduction of defect energy at the surface is stronger for individual  $Co_{Li}^+$  defect, its formation will be energetically favorable, explaining reconstruction effects. However, this will require to consider charged slabs and to employ potential correction approaches as proposed by Freysoldt et al. [71], as well as to prevent electron escape to the vacuum.

Finally, it should be noted that from a computational point of view the study of the surface reconstruction with the DFT/DFT+U approach is significantly complicated by the fact that d-metals vary their orbital order, significantly affecting energetics. Since DFT+U does not guarantee the convergence to the lowest energy state, this degree of freedom requires a separate explicit search. To simplify that task we created special subroutines that allow introducing deformations to localize small polarons at bulk and surface as well as automatized creation of symmetrically non-equivalent antisite defect pairs, which are implemented in the SIMAN package [32].

## 7. Conclusions

Density functional theory calculations with Hubbard correction are used to study antisite defect pairs with small polarons (ASC) in the bulk and at the surface of four oxide materials used as cathodes in batteries:  $LiNiO_2$ ,  $LiCoO_2$ ,  $NaNiO_2$ , and  $NaCoO_2$ . To identify relevant surface orientations we construct Wulff crystal shapes depending on the Li and  $O_2$  chemical potentials taking into account non-stoichiometric polar surfaces.

Rhombohedral phases ( $LiNiO_2$ ,  $LiCoO_2$ ,  $NaCoO_2$ ) have similar Wulff shapes with (104) and (003) as the primary surfaces. The dependence of Wulff shape on chemical potential is moderate for Li-based oxides and weak for Na-based oxides. The monoclinic  $NaNiO_2$  phase has only non-polar  $(10\bar{1})_m$  and  $(111)_m$  surfaces (analogue of  $(104)_{hex}$ ) and no dependence on chemical potential. Due to the absence of Ni/Co–O broken bonds, the polar (003) surface is only slightly higher in energy than non-polar (104). Due to weaker bonds, the energies of the non-polar surfaces of Na-based and Ni-based oxides are smaller than those of Li-based and Co-based oxides. However, due to the larger polarity compensation of longer bonds the energies of polar surfaces are higher for Na-based oxides than those of Li-based oxides.

In  $LiCoO_2$  and  $NaCoO_2$  the exchange of  $A = Li$  or  $Na$  and  $Co$  causes a  $Co^{3+}$  disproportionation into  $Co^{2+}$  at the  $A$  site and  $Co^{4+}$  at neighboring  $M$  site with the formation of small hole polaron. The most stable position of the  $Co^{4+}$  is 1 NN from  $A_{Co}''$  and 3 NN from  $Co_A'$ . In  $NaNiO_2$  the Ni atom at the Na site is also in the + 2 state, while the + 4 state is delocalized. In  $LiNiO_2$  ( $P2/c$ ) with the  $Ni^{2+}/Ni^{4+}$  charge ordering, the exchange of  $Ni^{2+}$  and Li occurs without formation of a small hole polaron. For  $LiNiO_2$  and  $LiCoO_2$  the lowest formation energies of ASC are 0.62 and 1.8 eV, respectively. The  $M_A$  and  $A_M$  components prefer to be either at the 1 NN or 2 NN separations, 0.2 eV lower than at 3 NN. For  $NaNiO_2$  and  $NaCoO_2$  the lowest formation energies of ASC are 2.1 and 2.9 eV, respectively, for the 2 NN separation.

The surface and surface–subsurface ASC have noticeably lower energies than their bulk counterparts in the case of Co-based oxides. This is especially pronounced in  $NaCoO_2$ , where the ASC energy is reduced from 3.2 to 1.6 eV. We associate such a reduction with the easier relaxation and minimization of broken  $M$ –O bonds at the surface. In  $NaNiO_2$  the reduction of the ASC energy at the surface is only 0.3 eV (from 2.4 to 2.1 eV). The ASC related reconstruction at the (104) surface, studied with Monte-Carlo method, shows that no additional gain exists compared to individual surface antisite pairs.

Overall, the considered surface antisite complexes are shown to be energetically unstable defects suggesting that surface reconstruction may occur due to the change of the surface chemical composition, requiring further investigation of each type of the antisite defect and small polaron interaction with surfaces. This is justified by the discovered easier formation of antisite pairs at the surface, which can explain surface reconstruction during electrochemical cycling.

### CRediT authorship contribution statement

**A.O. Boev:** Data curation, Formal analysis, Investigation, Methodology, Software, Visualization, Writing - original draft. **S.S. Fedotov:** Formal analysis, Visualization, Writing - review & editing. **A.M. Abakumov:** Resources, Validation, Writing - review & editing. **K.J. Stevenson:** Resources, Validation, Writing - review & editing. **G. Henkelman:** Formal analysis, Resources, Validation, Writing - review & editing. **D.A. Aksyonov:** Conceptualization, Data curation, Formal analysis, Investigation, Methodology, Software, Visualization, Supervision, Writing - original draft, Writing - review & editing, Funding acquisition.

## Declaration of Competing Interest

The authors declare that they have no known competing financial interests or personal relationships that could have appeared to influence the work reported in this paper.

## Acknowledgments

D. Aksyonov and S. Fedotov acknowledge support from Russian Foundation for Basic Research, No. 18-33-00821. D. Aksyonov would like to thank I. Seymour for fruitful discussions.

## Appendix A. Supplementary material

Supplementary data associated with this article can be found, in the online version, at <https://doi.org/10.1016/j.apsusc.2020.147750>.

## References

- [1] A. Manthiram, J.C. Knight, S.-T. Myung, S.-M. Oh, Y.-K. Sun, *Adv Energy Mater.* 6 (2016) 1501010.
- [2] L. Chen, M. Fiore, J.E. Wang, R. Ruffo, D.-K. Kim, G. Longoni, *Adv. Sustain. Syst.* 2 (2018) 1700153.
- [3] N. Nitta, F. Wu, J.T. Lee, G. Yushin, *Mater. Today* 18 (2015) 252.
- [4] C. Julien, S. Gastro-Garcia, *J. Power Sources* 97 (2001) 290.
- [5] C.J. Orendorff, D.H. Doughty, *Electrochem. Soc. Interface* 21 (2012) 35.
- [6] G. Vallverdu, M. Minvielle, N. Andreu, D. Gonbeau, I. Baraille, *Surf. Sci.* 649 (2016) 46.
- [7] B. Xiao, X. Sun, *Adv. Energy Mater.* 8 (2018) 1802057.
- [8] N.H. Kwon, D. Mouck-Makanda, K.M. Fromm, *Batteries* 4 (2018) 50.
- [9] M. Park, X. Zhang, M. Chung, G.B. Less, A.M. Sastry, *J. Power Sources* 195 (2010) 7904.
- [10] M.D. Radin, S. Hy, M. Sina, C. Fang, H. Liu, J. Vinckeviciute, M. Zhang, M.S. Whittingham, Y.S. Meng, A. der Ven, *Adv. Energy Mater.* 7 (2017) 1602888.
- [11] B. Xu, C.R. Fell, M. Chi, Y.S. Meng, *Energy Environ. Sci.* 4 (2011) 2223.
- [12] U.-H. Kim, D.-W. Jun, K.-J. Park, Q. Zhang, P. Kaghazchi, D. Aurbach, D.T. Major, G. Goobes, M. Dixit, N. Leifer, et al., *Energy Environ. Sci.* 11 (2018) 1271.
- [13] S. Guo, Q. Li, P. Liu, M. Chen, H. Zhou, *Nat. Commun.* 8 (2017) 135.
- [14] J. Zhong, Z. Yang, Y. Yu, Y. Liu, J. Li, F. Kang, *Appl. Surf. Sci.* 512 (2020) 145741.
- [15] F. Lin, I.M. Markus, D. Nordlund, T.-C. Weng, M.D. Asta, H.L. Xin, M.M. Doeff, *Nat. Commun.* 5 (2014) 3529.
- [16] P. Yan, J. Zheng, J. Zheng, Z. Wang, G. Teng, S. Kuppen, J. Xiao, G. Chen, F. Pan, J.-G. Zhang, C.-M. Wang, *Adv. Energy Mater.* 6 (2016) 1502455.
- [17] H. Zhang, B.M. May, J. Serrano-Sevillano, M. Casas-Cabanas, J. Cabana, C. Wang, G. Zhou, *Chem. Mater.* 30 (2018) 692.
- [18] G. Li, Q. Li, L. Li, J. Fan, Q. Ge, D. Xie, J. Zheng, G. Li, *Appl. Surf. Sci.* 427 (2018) 226.
- [19] E. Cho, S.-W. Seo, K. Min, *ACS Appl. Mater. Interfaces* 9 (2017) 33257.
- [20] D. Kramer, G. Ceder, *Chem. Mater.* 21 (2009) 3799.
- [21] P. Yan, J. Zheng, D. Lv, Y. Wei, J. Zheng, Z. Wang, S. Kuppen, J. Yu, L. Luo, D. Edwards, et al., *Chem. Mater.* 27 (2015) 5393.
- [22] K. Hoang, M.D. Johannes, *J. Mater. Chem. A* 2 (2014) 5224.
- [23] H. Chen, J.A. Dawson, J.H. Harding, *J. Mater. Chem. A* 2 (2014) 7988.
- [24] M.S. Park, *Phys. Chem. Chem. Phys.* 16 (2014) 16798.
- [25] C. Liang, F. Kong, R.C. Longo, C. Zhang, Y. Nie, Y. Zheng, K. Cho, *J. Mater. Chem. A* 5 (2017) 25303.
- [26] C. Liang, R.C. Longo, F. Kong, C. Zhang, Y. Nie, Y. Zheng, K. Cho, *ACS Appl. Mater. Interfaces* 10 (2018) 6673.
- [27] K. Hoang, M.D. Johannes, *J. Phys.: Condens. Matter* 30 (2018) 293001.
- [28] K. Hoang, M. Johannes, *Chem. Mater.* 28 (2016) 1325.
- [29] Y. Kim, *Phys. Chem. Chem. Phys.* 21 (2019) 24139.
- [30] J. Zheng, Y. Ye, T. Liu, Y. Xiao, C. Wang, F. Wang, F. Pan, *Acc. Chem. Res.* 52 (2019) 2201.
- [31] R. Kaushalya, P. Iyngaran, N. Kuganathan, A. Chronos, *Energies* 12 (2019) 3094.
- [32] <https://github.com/dimonaks/siman/wiki>.
- [33] G. Kresse, J. Furthmüller, *Comput. Mater. Sci.* 6 (1996) 15.
- [34] D.A. Aksyonov, S.S. Fedotov, K.J. Stevenson, A. Zhugayevych, *Comput. Mater. Sci.* 154 (2018) 449.
- [35] J. Perdew, K. Burke, M. Ernzerhof, *Phys. Rev. Lett.* 77 (1996) 3865.
- [36] S.L. Dudarev, G.A. Botton, S.Y. Savrasov, C.J. Humphreys, A.P. Sutton, *Phys. Rev. B* 57 (1998) 1505.
- [37] A. Jain, G. Hautier, C.J. Moore, S. Ping Ong, C.C. Fischer, T. Mueller, K.A. Persson, G. Ceder, *Comput. Mater. Sci.* 50 (2011) 2295.
- [38] W. Sun, G. Ceder, *Surf. Sci.* 617 (2013) 53.
- [39] G. Wulff, *Zeitschrift für Kristallographie-Crystalline Materials* 34 (1901) 449.
- [40] R.V. Zucker, D. Chatain, U. Dahmen, S. Hagège, W.C. Carter, *J. Mater. Sci.* 47 (2012) 8290.
- [41] L. Wang, T. Maxisch, G. Ceder, *Phys. Rev. B* 73 (2006) 195107.
- [42] M.K. Aydinol, A.F. Kohan, G. Ceder, K. Cho, J. Joannopoulos, *Phys. Rev. B* 56 (1997) 1354.
- [43] C. Liu, Z.G. Neale, G. Cao, *Mater. Today* 19 (2016) 109.
- [44] S.P. Ong, L. Wang, B. Kang, G. Ceder, *Chem. Mater.* 20 (2008) 1798.
- [45] S.P. Ong, A. Jain, G. Hautier, B. Kang, G. Ceder, *Electrochem. Commun.* 12 (2010) 427.
- [46] S.P. Ong, W.D. Richards, A. Jain, G. Hautier, M. Kocher, S. Cholia, D. Gunter, V.L. Chevrier, K.A. Persson, G. Ceder, *Comput. Mater. Sci.* 68 (2013) 314.
- [47] S. Yamada, M. Fujiwara, M. Kanda, *J. Power Sources* 54 (1995) 209.
- [48] H. Chen, C.L. Freeman, J.H. Harding, *Phys. Rev. B* 84 (2011) 85108.
- [49] H.J. Orman, P.J. Wiseman, *Acta Crystallogr. Sect. C* 40 (1984) 12.
- [50] T. Ohzuku, A. Ueda, *J. Electrochem. Soc.* 141 (1994) 2972.
- [51] S. Dick, M. Müller, F. Preissinger, T. Zeiske, *Powder Diffr.* 12 (1997) 239.
- [52] P. Vassilaras, X. Ma, X. Li, G. Ceder, *J. Electrochem. Soc.* 160 (2013) A207.
- [53] E. Chappel, M.D. Núñez-Regueiro, G. Chouteau, O. Isnard, C. Darie, *Eur. Phys. J. B – Condens. Matter Complex Syst.* 17 (2000) 615.
- [54] L. Viciu, J.-W.G. Bos, H.W. Zandbergen, Q. Huang, M.L. Foo, S.d. Ishiwata, A.P. Ramirez, M. Lee, N.P. Ong, R.J. Cava, *Phys. Rev. B* 73 (2006) 174104.
- [55] C. Fouassier, G. Matejka, J.M. Reau, P. Hagenmuller, *J. Solid State Chem.* 6 (1973) 532.
- [56] Y. Takahashi, Y. Gotoh, J. Akimoto, *J. Solid State Chem.* 172 (2003) 22.
- [57] Q. Huang, M.L. Foo, R.A. Pascal Jr, J.W. Lynn, B.H. Toby, T. He, H.W. Zandbergen, R.J. Cava, *Phys. Rev. B* 70 (2004) 184110.
- [58] R. Berthelot, D. Carlier, C. Delmas, *Nat. Mater.* 10 (2011) 74.
- [59] Y. Lei, X. Li, L. Liu, G. Ceder, *Chem. Mater.* 26 (2014) 5288.
- [60] T. Ohzuku, A. Ueda, M. Nagayama, Y. Iwakoshi, H. Komori, *Electrochim. Acta* 38 (1993) 1159.
- [61] B. Meredig, A. Thompson, H.A. Hansen, C. Wolverton, A. Van De Walle, *Phys. Rev. B – Condens. Matter Mater. Phys.* 82 (2010) 2.
- [62] L. Hong, L. Hu, J.W. Freeland, J. Cabana, S. Ögüt, R.F. Klie, *J. Phys. Chem. C* 123 (2019) 8851.
- [63] J.A. Santana, J. Kim, P.R.C. Kent, F.A. Reboredo, *J. Chem. Phys.* 141 (2014) 164706.
- [64] Y. Kim, H. Lee, S. Kang, *J. Mater. Chem.* 22 (2012) 12874.
- [65] N.G. Hormann, A. Gross, *ChemPhysChem* 15 (2014) 2058.
- [66] H. Cao, B. Xia, N. Xu, C. Zhang, *J. Alloys Compds.* 376 (2004) 282.
- [67] R.D. Shannon, *Acta Crystallogr. Sect. A: Cryst. Phys. Diffraction, Theoret. Gen. Crystallogr.* 32 (1976), p. 751.
- [68] J. Zheng, G. Teng, C. Xin, Z. Zhuo, J. Liu, Q. Li, Z. Hu, M. Xu, S. Yan, W. Yang, *J. Phys. Chem. Lett.* 8 (2017) 5537.
- [69] A.W. Moses, H.G.G. Flores, J.-G. Kim, M.A. Langell, *Appl. Surf. Sci.* 253 (2007) 4782.
- [70] A. Abbaspour-Tamijani, J.W. Bennett, D.T. Jones, N. Cartagena-Gonzalez, Z.R. Jones, E.D. Laudadio, R.J. Hamers, J.A. Santana, S.E. Mason, *Appl. Surf. Sci.* 515 (2020) 145865.
- [71] C. Freysoldt, J. Neugebauer, *Phys. Rev. B* 97 (2018) 205425.